High-Resolution Raman-OTDR Distributed Temperature Sensors Based on Fast-Non Local Means Denoising Algorithm

Ziheng Yan, Bin Du, Zhuoda Li, Canxiong Chen, Baijie Xu, Xizhen Xu, George Y. Chen, Senior Member, IEEE, Senior Member, Optica, Yiping Wang, Senior Member, IEEE, Fellow, OSA, and Jun He, Member, IEEE, Member, OSA

Abstract—Raman-optical time domain reflectometry (R-OTDR) -based distributed temperature sensing (DTS) with high temperature resolution is of great significance in extremely harsh environment of deep wellbore. In this work, we experimentally demonstrate a Fast-non local means (Fast-NLM) algorithm for performance improvement without modifying the hardware architecture of a conventional R-OTDR system. In the proposed method, the first-in-first-out (FIFO) data transmission protocol is used to reconstruct the two-dimensional (2D) temperature image in real time. An integral image is employed to simplify the calculation of Euclidean distance between similarities in the 2D space-time domain. The overall response time by using the method decreases from 27.9 s to 1.7 s, marking a 16-fold enhancement over traditional NLM denoising methodologies. An average temperature resolution is below 0.01 °C at the end of fiber. The evolution of the measured temperature at the hot spot position does not produce delay or distortion. Moreover, two segments fiber at 300 m and 9.68 km are rigorously tested with the temperature range from 50 °C to 300 °C and time span of 4 hours, compared with conventional wavelet denoising algorithm, the root means square error decrease from 1.02 °C to 0.42 °C. In all, the Fast-NLM denoising based R-OTDR illustrates great improvement in temperature resolution while maintaining fast response time. This achievement holds immense potential for

Received 21 April 2025; revised 11 July 2025; accepted 10 August 2025. Date of publication 13 August 2025; date of current version 2 October 2025. This work was supported in part by the National Key Research and Development Program of China under Grant 2023YFB3208600, in part by the National Natural Science Foundation of China (NSFC) under Grant 62222510, Grant 62435012, and Grant 62205225, in part by the Department of Science and Technology of Guangdong Province under Grant 2022B1515120050, in part by China Postdoctoral Science Foundation under Grant 2024M762125, and in part by the Ling Chuang Research Project of China National Nuclear Corporation under Grant CNNC-LCKY-202259. (Corresponding authors: Bin Du; Jun He.)

The authors are with the State Key Laboratory of Radio Frequency Heterogeneous Integration, Key Laboratory of Optoelectronic Devices and Systems of Ministry of Education/Guangdong Province, College of Physics and Optoelectronic Engineering, Shenzhen University, Shenzhen 518060, China, and also with the Shenzhen Key Laboratory of Photonic Devices and Sensing Systems for Internet of Things, Guangdong and Hong Kong Joint Research Centre for Optical Fiber Sensors, Shenzhen University, Shenzhen 518060, China (e-mail: 2210452115@email.szu.edu.cn; dubin2016@email.szu.edu.cn; 2100453028@email.szu.edu.cn; 2410232018@mails.szu.edu.cn; 1900453046@email.szu.edu.cn; xizhenxu@szu.edu.cn; gychen@szu.edu.cn; ypwang@szu.edu.cn; hejun

07@szu.edu.cn).

Color versions of one or more figures in this article are available at https://doi.org/10.1109/JLT.2025.3598263.

Digital Object Identifier 10.1109/JLT.2025.3598263

diverse applications, including dynamic monitoring in the realms of energy development, oil and gas exploration, and allied fields.

Index Terms—Distributed optical fiber sensing, Raman OTDR, Fast-NLM, high temperature resolution.

I. INTRODUCTION

ISTRIBUTED optical fiber sensors (DOFS) [1], [2], known for their compact structure, corrosion resistance, and immunity to electromagnetic interference [3], are ideal for measuring physical quantities in various environments [4], [5], [6]. These advantages have sparked significant interest across multiple domains [7], [8]. Among these sensing technologies, Raman scattering-based optical fiber distributed temperature sensing (DTS), standing as the most mature and stable longdistance distributed temperature sensing technique, is receiving extensive attention in oil and gas exploration sensing [9], real-time power line monitoring [10], [11], and other distributed temperature monitoring fields [12], [13]. The performance metrics of the Raman DTS system typically encompass temperature accuracy and precision, spatial resolution, as well as sensing distance. Significantly, improving the accuracy and resolution of temperature measurement constitutes a substantial challenge. This is attributed to the fact that the backscattered light signal in the Raman system is approximately 60-70 dB inferior in strength compared to the incident pulse power [1], [9]. Moreover, the Anti-Stokes signal, which exhibits better temperature sensitivity, is around 4 dB lower than the Stokes signal and thus more susceptible to noise contamination from auxiliary equipment. Consequently, the typical signal of the Raman DTS exhibits a relatively lower signal-to-noise ratio (SNR), thereby leading to lower accuracy and precision.

SNR improvement or noise suppression could improve the temperature accuracy and resolution of the Raman system. Over recent decades, various methods for SNR improvement and noise suppression such as the Anti-Stokes demodulation approach, optical pulse coding [14], wavelet denoising [15], and Fourier transform [16], have been demonstrated for performance improvements [17]. In 2012, Soto M. et al. [18] employed the Anti-Stokes demodulation method within the dual-terminal Raman-DTS system. The demodulation temperature accuracy improved from 1.5 °C to 1.1 °C. Nevertheless, this method is

0733-8724 © 2025 IEEE. All rights reserved, including rights for text and data mining, and training of artificial intelligence and similar technologies. Personal use is permitted, but republication/redistribution requires IEEE permission. See https://www.ieee.org/publications/rights/index.html for more information.

susceptible to environmental fluctuations, and its improvement effect is limited. In 2017, Vazquez G. et al. [19] demonstrated a pseudo-random pulse sequence optical pulse coding and deconvolution algorithms, with temperature resolution of 1.5 °C at a spatial resolution of 2 m. In 2019, Li et al. [20] demonstrated a cumulative average, differential temperature compensation, and wavelet transform modulus maxima method for the Raman signal and temperature signal denoising. The accuracy improves from 15 °C to 0.56 °C along the 10.8 km. These methods increase the complexity of the system, while improving the SNR, thereby raising the hardware cost of the sensor. Besides, the combination of these signal denoising techniques can further improve the SNR and spatial resolution [21], [22], [23] although the configuration cost would increase due to the complexity of demodulation.

Image denoising technology, such as non-mean [24] and bilateral filter method [25], illustrates an effective method for performance improvement in DOFS. The non-mean filter method effectively preserves image details during noise reduction but it may generate artifact in homogeneous regions. And the bilateral filter, integrating spatial and intensity information, is highly sensitive to parameter selection and incurs high computational costs. One significant advancement is the successful application of the Non-Local Means (NLM) algorithm from image processing techniques to DOFS [26]. This approach fully leverages the high similarity and redundancy contained in the one-dimensional information obtained from distributed Raman sensors, resulting in a significant enhancement of the temperature resolution. Despite these advancements, the computational time of the NLM algorithm is still a formidable task [27], [28], [29]. It remains a big challenge to realize a reliable distributed high-temperature sensing system that offers long-distance sensing, high temperature, high speed, and temperature resolution simultaneously. The computational demands of the NLM algorithm can hinder its practical application in real-time or near-real-time monitoring

In this article, we demonstrate a Fast-NLM-based real-time denoising algorithm specifically tailored to Raman DTS signals without modifying the hardware architecture of a conventional R-OTDR system. In proposed algorithms, the 2D temperature image is real-timely reconstructed by utilizing a FIFO data transmission protocol and using integral image technique to accelerate calculation. Compared to the traditional algorithm, the system's time consumption, the temperature resolution, the delay characteristics, and the long-term stability are analyzed by using the oil bath furnace. The experimental results show an average temperature resolution of 0.01 °C at the end of the fiber. Compared with the wavelet denoising (WD) algorithm, the temperature accuracy is improved from 1.59 °C to 0.39 °C. Furthermore, the long-term stability over 4 hours measurement shows the root mean square error (RMSE) of the Fast-NLM decrease from 1.02 °C to 0.42 °C, and the maximum deviation decrease from 3.36 °C to 0.88 °C, at 300 °C, respectively. As a result, the remarkable denoising performance makes it highly suitable utilization for DTS in oil and gas, power, smelting, and aviation industries.

II. PRINCIPLES OF OPERATION

A. The Principle of Raman Temperature Demodulation

In the R-OTDR system, spatial positioning is carried out by the time-of-flight of the spontaneous Raman scattering light, while the temperature is determined by analyzing their intensity variations. The temperature sensitivity of Raman scattering originates from the thermally modulated vibrational energy states of silica molecules. In addition the interaction between photons and thermally moving chemical bonds produces Raman scattering Anti-Stokes and Stokes photons. The strength of the signal as function of temperature T (in Kelvin) was expressed as:

$$\frac{P_{as}(T)}{P_s(T)} = \frac{K_{as}}{K_s} \left(\frac{v_{as}}{v_s}\right)^4 \exp\left(\frac{h\Delta v}{k_B T}\right) \exp\left[\left(\alpha_s - \alpha_{as}\right)L\right],\tag{1}$$

where $P_{as}(T)$ ($P_s(T)$) is the power of Anti-Stokes (Stokes) light in temperature (T), K_{as} (K_s) is the scattering coefficient of the Anti-Stokes (Stokes) light, which is related to the scattering cross section. The v_{as} (v_s) is the optical frequency of Anti-Stokes (Stokes) light, α_{as} (α_s) is the transmission loss of Anti-Stokes (Stokes) light in the fiber, h is the Planck constant, k_B is the Boltzmann constant, and $\triangle v$ is the frequency difference between the upper and lower energy levels of the Raman scattering spectrum.

As given the reference temperature T_{θ} in Raman DTS, the demodulated temperature using the Anti-Stokes light and Stokes light generated by the spontaneous Raman backscattering effect, could generally be expressed as:

$$T = \left\{ \frac{1}{T_0} - \frac{k_B}{h\Delta v} \left[\ln \frac{P_{as}(T) \cdot P_s(T_0)}{P_{as}(T_0) \cdot P_s(T)} \right] \right\}^{-1}$$
$$= \left\{ \frac{1}{T_0} - \frac{k_B}{h\Delta v} \left[\ln \frac{R(T)}{R(T_0)} \right] \right\}^{-1}. \tag{2}$$

Compared with the single-way demodulation methods (i.e., demodulated by Anti-Stokes signal) in [14], the two-way method (i.e., (2)) with two-way light ratio could enhance the stability of the DTS system and other factors.

B. The Principle of Fast-NLM Method

The Fast-NLM method achieves fast 2D image reconstruction using FIFO data queues, integral image technology and achieves noise reduction using the high degree of similarity and redundancy within the image. In the DTS, the temperature change trend among adjacent sensing points is highly correlated (spatial similarity). The temperature fluctuation patterns at the same location at different times may repeat (time similarity). Abnormal events (such as fires) exhibit similar local hotspot diffusion patterns in the space-time map (Structural similarity). The unique advantages of this algorithm in processing temperature data are as follows: anti-local mutation interference and single-point noise are effectively suppressed through non-local similar block weighting. Similar thermal diffusion patterns in different time slices can be identified due to cross-temporal correlation enhancement. And the algorithm pre-calculates the cumulative sum of storage (the original image is calculated as

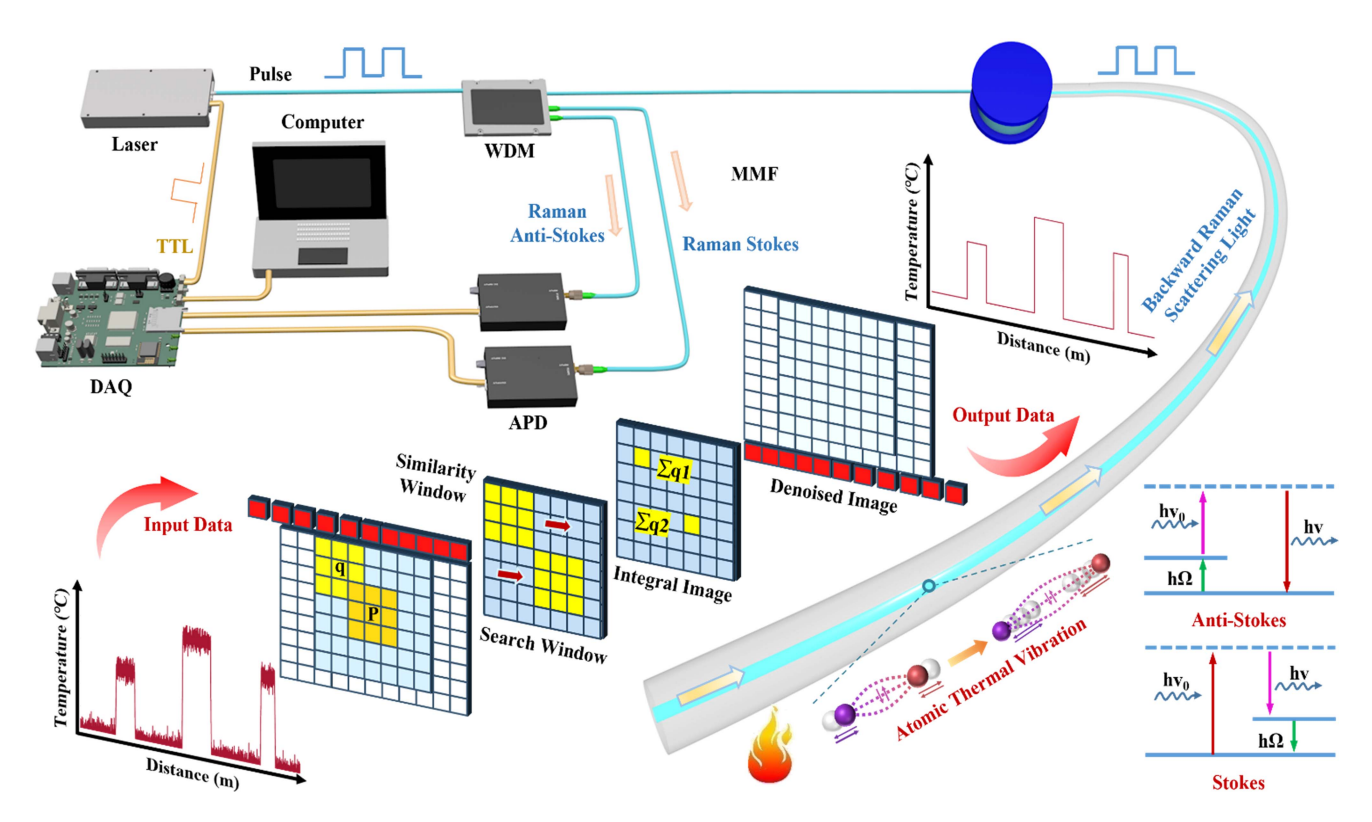


Fig. 1. Schematic diagram of Raman distributed temperature sensing system and denoising algorithm.

an integral image) by the integral image technology to avoid point-by-point calculations. This ensures a fast response time while effectively achieving denoising.

The whole algorithm denoising process is shown in Fig. 2(a). In step 1, the 2D imagination data reconstructed by the FIFO data queues. An optical fiber temperature data graph at ambient temperature is simulated in advance. The one-dimensional original signal is embedded at the top of the two-dimensional temperature data image. In step 2, slide the similarity window in the search window and calculate the Euclidean distance between the two similarity windows. Firstly, a search window $R \times R$ ($R = 2R_s + 1$, R_s is the radius of search window) centered on the target pixel p, and a similarity window $r \times r$ ($r = 2r_s + 1$, r_s is the radius of similarity window) sliding within the search window are applied to the 2D signal. The Euclidean distance $||V(p) - V(q1)||^2$, between the two similarity windows centered on p and q1, is calculated as follows:

$$||V(p) - V(q1)||^2 = \frac{1}{r^2} \Sigma ||b(p+s) - b(q1+s)||^2.$$
 (3)

Where *s* is the sampling interval. In this work, when repeatedly calculating the Euclidean distance for temperature pixel values, we employ integral image technology to significantly reduce the computational burden and enhance the calculation speed.

In step 3, weights are calculated based on the similarity derived from the Euclidean distance. First, the similarity W(p, q1) is determined by the distance between the rectangular similarity windows centered on p and q1:

$$W(p,q1) = \frac{1}{Z(p)} \exp\left(-\frac{||V(p) - V(q1)||^2}{g^2}\right).$$
 (4)

Here, parameter g is the smoothing parameter, which plays a crucial role in regulating the attenuation of the function. As g increases, the transformation of the Gaussian function becomes smoother. Conversely, when g decreases, a larger proportion of edge-detail components are retained. However, this reduction may lead to an excessive number of noise points remaining.

In step 4, the noisy image n is calculated from the denoised image b:

$$n(p) = \sum W(p, q1) \cdot b(q1). \tag{5}$$

In step 5, the integral image technique is used to simplify the calculation. A two-dimensional integral image is constructed and pre-store the cumulative square sum for each position, as shown in Fig. 2(b4). I(i, j) represent a pixel point in the original image, while x and y denote the dimensions of the original region. Q(x, y) is used to calculate the sum of pixels within a specific rectangular region of the temperature map

$$Q(x,y) = \sum_{i \le x, j \le y} I(i,j)^{2}.$$
 (6)

In step 6, the processed data are normalized through weighted averaging of pixel values for all temperature data points within the search window. Additionally, edge areas of the image are filled to prevent boundary crossing in the integral image,

$$\hat{I}(p) = \frac{\sum W(p, q1) \cdot I(q1)}{\sum W(p, q1)}.$$
 (7)

Through this procedure, the denoised image is generated.

Finally, in step 7, one-dimensional temperature data are extracted from the denoised image in order. As shown in Fig. 2(b5)

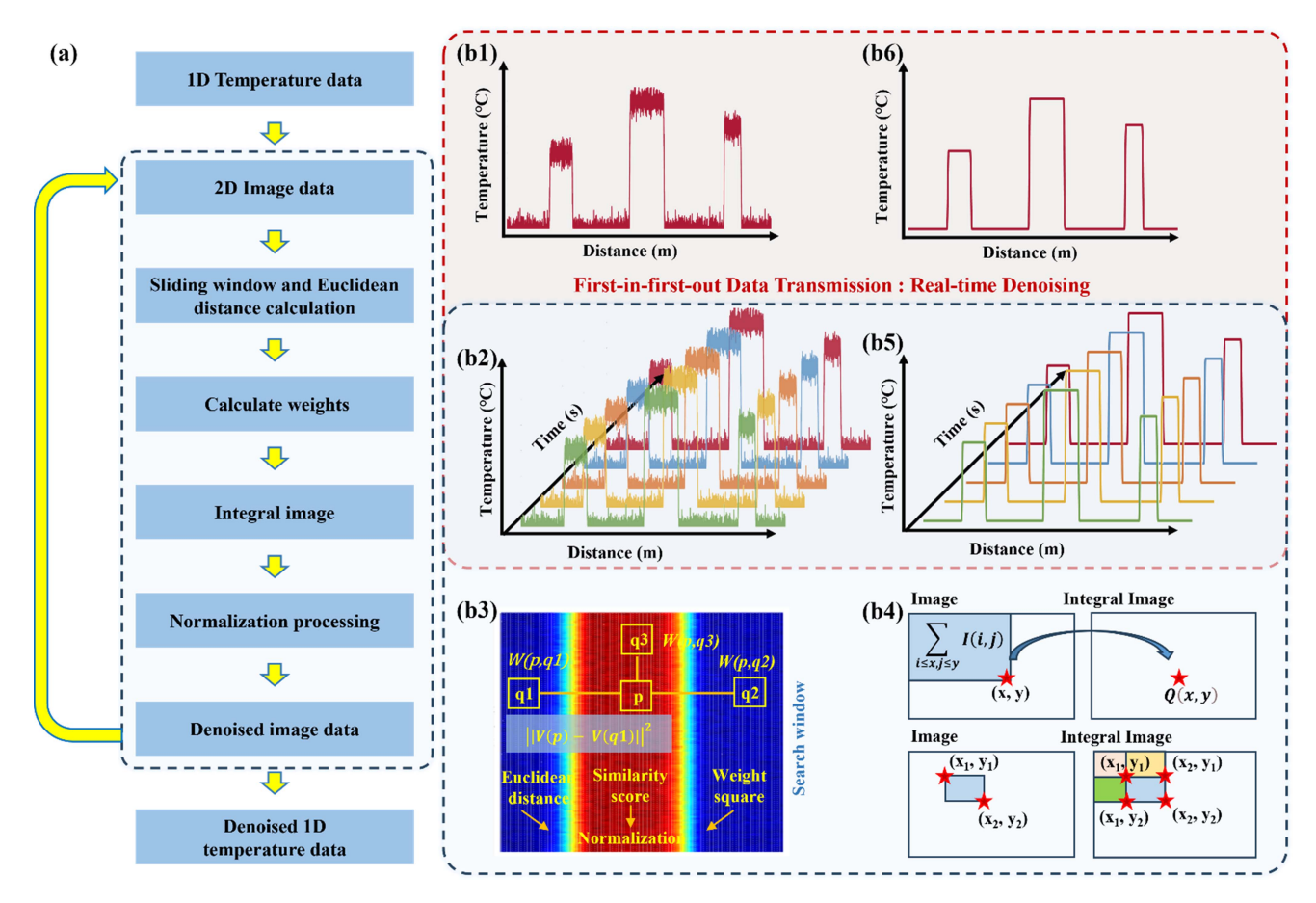


Fig. 2. Schematic of the Fast-NLM-based denoising method for DTS. (a) The denoising process; (b1) noisy 1D temperature data; (b2) image data composed of noisy 1D temperature data; (b3) definition of the similarity window, the search window, the filter parameter, the weight, and similarity calculated using Euclidean distance; (b4) the integral image used for calculating the pixel spacing of the original image; (b5) the denoised image data; (b6) the denoised 1D temperature data.

and (b6), continuity is maintained across both temporal and spatial dimensions.

III. EXPERIMENTS AND RESULTS

The configuration of the Raman-DTS system is depicted in Fig. 1. The system comprises a distributed feedback laser (1550 nm, 8 ns), a wavelength division multiplexer (WDM), a highspeed data acquisition card (DAQ), two avalanche photodiodes (APDs), and a personal computer. The fiber under test (FUT) in the experiments is a graded-index multimode fiber (50/125, MMF). The laser pulses, with a peak optical power of 13.5 W and a repetition rate of 10 kHz, launch into the FUT via the WDM. As the light pulse propagates through the FUT, spontaneous Raman backscattering light produced while the probe light interacts with the fiber core. These optical signals are filtered by the WDM and subsequently converted into electrical signals by the APD. The electrical signals are then collected by DAO and transmitted to the computer, configured with a 2.3-GHz processor and 8 GB of RAM. Within this computational environment, demodulation and image-based denoising procedures are implemented to reconstruct the temperature curve. Besides, a high-precision second-class platinum resistance thermometer and an oil bath furnace are used to conduct the high-temperature experiments.

At first, the Fast-NLM algorithm for DTS was optimized. A fiber segment with length of 10 m at 9.68 km are heated from ambient to 60 °C. Fig. 3 illustrates the optimization results of the signal from this segment. As shown in Fig. 3(a1), the spatial-temporal temperature curve varies as the similarity window widths increase from 5 to 21. It should be noted that the spatial resolution is quantified by the positions corresponding to 10% to 90% response in the temperature profile. As shown in Fig. 3(a2) and (a3), the spatial resolution and temperature resolution both degrade as the increasing window width smooths the rising edge, confirming a more optimal spatial and temperature scale fidelity with a smaller window width. As shown in Fig. 3(a4), the response time gradually increases from 1.8 s to 3.0 s with expanding similarity window width, indicating that larger window widths may result in slower responses. As a result, to obtain better performance, the similarity window widths are better to be the minimum. Under this condition, the spatial resolution, the temperature resolution, and the response time are optimized to 2.5 m, 0.06 °C, and 1.8 s, respectively.

The magnitude of the search window plays a pivotal role in system-related processing time. As shown in Fig. 3(b1), the spatial-temporal temperature curve varies as the search window widths increase from 9 to 33. The variation of spatial-temporal resolution versus search window widths is illustrated in

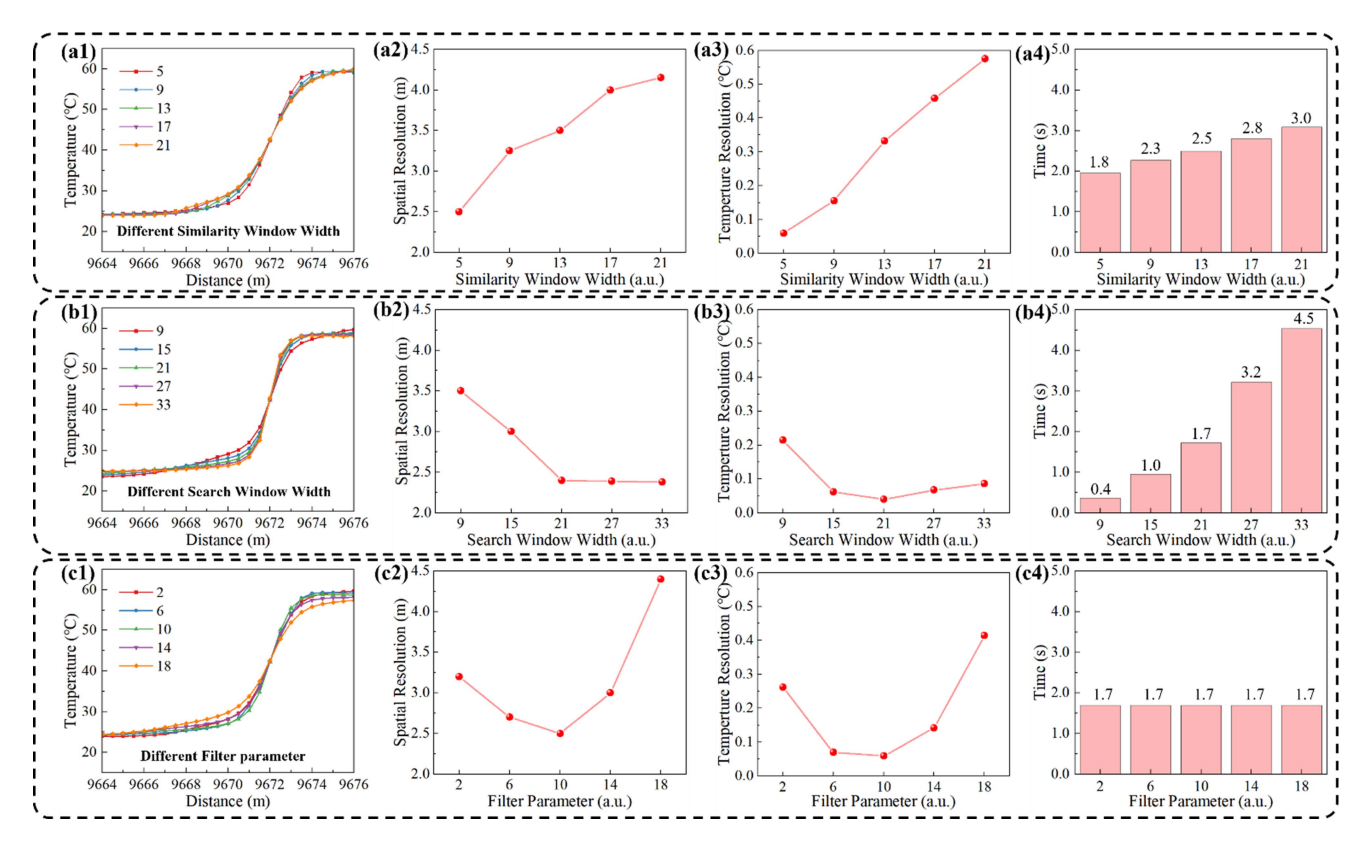


Fig. 3. Measured results of R-DTS using Fast-NLM algorithm for temperature denoising. (a1), (b1), and (c1) The denoised temperature curves using three varying parameters (similarity window width, search window width, and filter parameter, respectively). (a2), (b2), and (c2) The influences on spatial resolution. (a3), (b3), and (c3) The influences on temperature resolution. (a4), (b4), and (c4) The influences on response time.

Fig. 3(b2). As the search window width incrementally increases, the spatial resolution illustrates a decline-stabilization pattern trend. As the search window width incrementally expands to 21, the spatial resolution reaches a minimum of 2.5 m. As shown in Fig. 3(b3), the temperature resolution illustrates a falling-thenrising trend as search window width increases. when the search window width incrementally expands to 21, the temperature resolution reaches minimal of 0.06 °C. As shown in Fig. 3(b4), the response time (in seconds) increased from 0.4 to 4.5 seconds. To obtain the better performance, the search window widths is better to be set as 21, while the spatial resolution, the temperature resolution, and the response time are optimized to 2.5 m, 0.06 °C, and 1.7 seconds, respectively.

The selection of an appropriate filter coefficient is particularly significant in the algorithmic processing. Suboptimal filter coefficients lead to insufficient noise reduction, whereas supra-threshold coefficients induce twofold degradation: spatial resolution deterioration and temperature measurement distortion due to over-smoothing. The systematic evaluation of filter parameters from 2 to 18 is shown in Fig. 3(c1)–(c4). As predictably shown in Fig. 3(c2) and (c3), both the temperature resolution and spatial resolution display a falling-then-rising trend. When the filter is 10, optimal spatial resolution and temperature resolution are optimized to be 2.5 m and 0.06 °C, respectively. Besides, filter parameter variations exert negligible impact on the response time (1.7 seconds). Taking all into account, the optimal similarity window width, search window width, and filter parameter are 5, 21, 10, respectively.

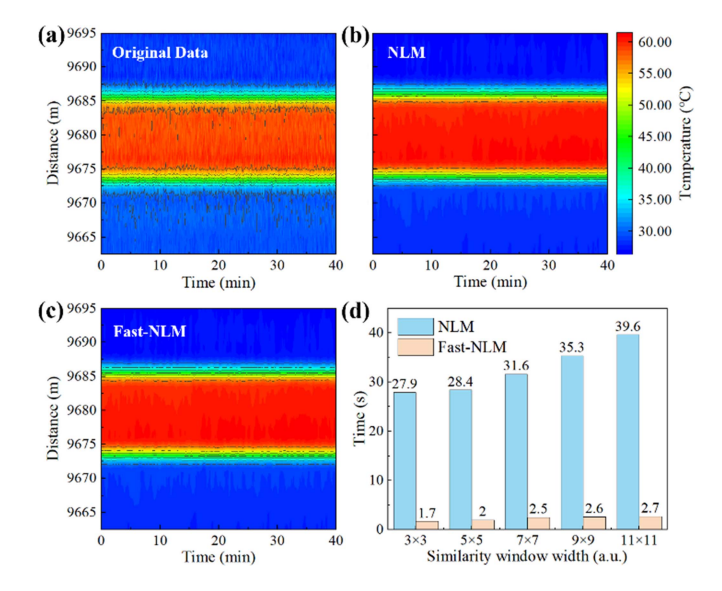


Fig. 4. The 2D spatiotemporal images using different denoising methods. (a) The original data; (b) 2D image data processed by NLM algorithm; (c) 2D image data processed by Fast-NLM algorithm. (d) The processing time of the conventional NLM algorithm and optimized Fast-NLM algorithm.

The computational time of the proposed method and the traditional NLM method are compared. Fig. 4(a)–(c) illustrate the consecutive 2D temperature image of the sensing fiber at heating temperature of 60 °C with a time span of 40 minutes. The temperature image data are processed by the 2D NLM and Fast-NLM

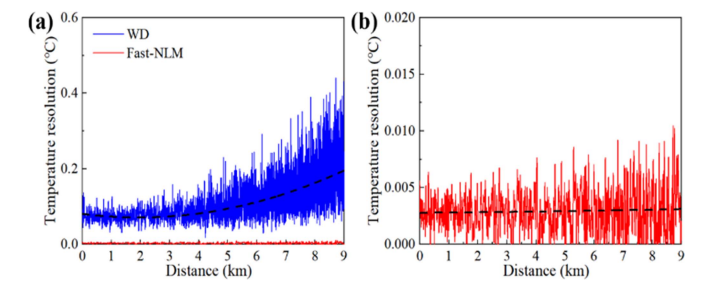


Fig. 5. (a) The temperature resolution as functions of distance by using the WD and Fast-NLM algorithms. (b) The variation in temperature resolution versus distance by using the Fast-NLM algorithm.

algorithm shown in Fig. 4(b) and (c). Compared with the original data in Fig. 4(a), the data processed by these two algorithms curtail the temperature fluctuation from 1.59 °C to 0.39 °C. As depicted in Fig. 4(d), a comparison of the computation times (in seconds) is made under disparate similarity window sizes. Thanks to integral image technology, the processing time is substantially curtailed without appreciably compromising the denoising capabilities of the algorithm. For all window sizes, the Fast-NLM algorithm demands significantly less computation time (1.7 s \sim 2.7 s) than the NLM algorithm (27.9 s \sim 39.6 s). This empirical finding indubitably demonstrates that the proposed Fast-NLM algorithm is more efficient in terms of computational resources. Under the precondition of noise reduction and data quality assurance, this efficiency is a highly pivotal factor for large-scale temperature data processing or real-time applications engendered by long-distance optical fiber.

The improvement in temperature resolution of the proposed method verifies the traditional WD method. Taking temperature resolution and temperature fluctuations into account, the optimal wavelet function, decomposition level and threshold are coif5, 4, Heursure, respectively. Fig. 5 illustrates the performance of the newly proposed Fast-NLM algorithm in comparison to the WD algorithm. As shown Fig. 5(a), a total distance spans a measured distance of 9 km. As the distance increases, the signal-to-noise ratio gradually deteriorates due to the continuous attenuation of the pump light and the scattering signal. As a result, the measured temperature resolution shows an upward and fluctuating trend. Compared with the WD algorithm (depicted by the blue curve), the Fast-NLM algorithm (represented by the red curve) indicates stable and significantly lower the temperature resolution. As shown in Fig. 5(b), compared with the WD method, the Fast-NLM algorithm improves the temperature resolution from 0.42 °C to 0.01 °C, indicating a remarkable improvement.

To validate the temperature sensing performance of the algorithm, the optical fiber is positioned in a normal temperature environment. A segment fiber of 15 m at 9602 m is put into a high temperature oil bath. The temperature of the bath is set to be 60 °C. Fig. 6(a) illustrates the temperature distribution of the whole fiber using three specific algorithms: WD algorithm (blue curve), NLM algorithm (green curve), and Fast-NLM algorithm (orange curve). The illustrations enlarge the local section spanning 8.5 km to 9 km. Compare with the WD algorithm, the data processed by the NLM and Fast-NLM algorithm curtails the

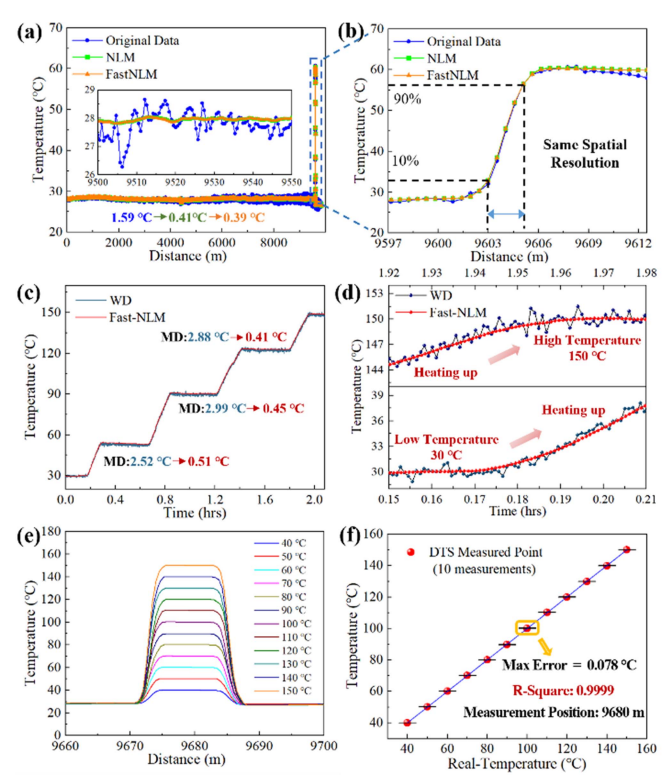


Fig. 6. The sensing performance of R-DTS using Fast-NLM method. (a) Denoising temperature curves using WD, NLM, and Fast-NLM methods, respectively. (b) Zoom-in of (a) at a specific region of 9597-9612 m. (c)The evolution of measured temperature from 30 °C to 150 °C with a time span of two hours. (d) Zoom-in of (c) at 0.15 - 0.21 h and 1.92 -1.98 h. (e) The measured temperature distribution in the heated region, from 40 °C to 150 °C with an interval of 10 °C. (f) The R-DTS measured temperatures as a function of referenced temperatures at 9680 m and the max error is 0.078 °C (standard deviation of 10 measurements).

temperature fluctuation from 1.59 °C to 0.41 °C and 0.39 °C. As shown Fig. 6(b), the spatial resolution remains 2 m without any deterioration. The results demonstrate that the denoising process produces no perceptible loss of spatial resolution.

The proposed method's real-time response was evaluated. Temperature in the bath is heating up from 30 °C to 150 °C with a timespan of two hours. At each constant temperature setpoint, the holding time is 0.4 hours. Fig. 6(c) displays the uninterrupted temperature evolution using the WD and Fast-NLM algorithms method. Across multiple constant temperature setpoints (50 °C, 90 °C, and 130 °C), the proposed WD method displays the maximum deviation (MD) values of 2.52 °C, 2.99 °C, and 2.88 °C, respectively. In stark contrast, the Fast-NLM algorithm demonstrated significantly reduced MDs of 0.51 °C, 0.45 °C, and 0.41 °C, respectively, representing a 6.5-fold improvement over WD. Additionally, the details of the turning point at 30 °C and 150 °C is illustrated in Fig. 6(d). The simultaneous turning of the red (Fast-NLM) and blue (WD) curves indicates that the algorithm has excellent real-time response characteristics. The temperature was then incrementally elevated from 40 °C to 150 °C in steps of 10 °C at 9.68 km. As shown in Fig. 6(e), 10 measurements were taken at each temperature point under various heating conditions to minimize the impact of the device's inherent fluctuations. The average temperature distribution

0.23

0.65

9.68

[16]

[36]

THICAL ALGORITHM DENOISING SCHEMES AND DATERIMENTAL RESULTS OF K-OTDK DASED DISTRIBUTED TEMPERATURE SENSORS				
Scheme	Distance (km)	Temperature accuracy (°C)	Temperature range (°C)	Reference
Dynamic sampling correction scheme	20.0	1.00	-25.0-45.0	[34]
D-SVD algorithms	0.60	0.87	45.2-60.0	[21]
Deep one-dimensional denoising CNN	10.0	0.70		[35]
Javelet transform modulus maxima method	10.8	0.56	42 6-90 6	[20]

0.50

0.30

0.39

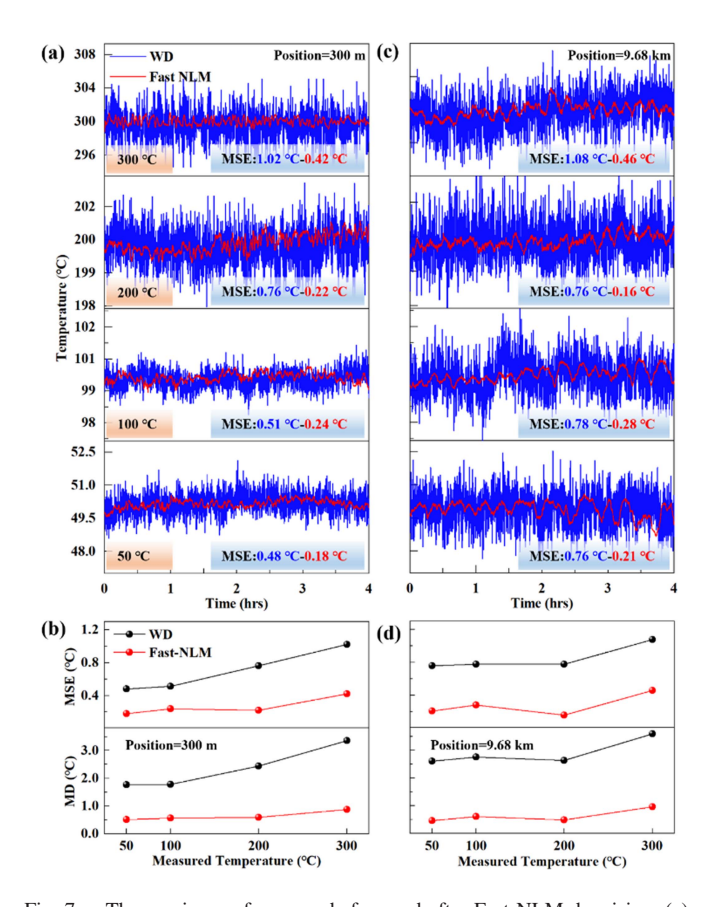
TABLE I
TYPICAL ALGORITHM DENOISING SCHEMES AND EXPERIMENTAL RESULTS OF R-OTDR BASED DISTRIBUTED TEMPERATURE SENSORS

reveals a flat curve in the heating region. As shown in Fig. 6(f), at the 9680 m position of the optical fiber, the measurement error is less than 0.078 °C (maximum value) after calculating data 10 times across multi-temperature points ranging from 40 °C to 150 °C. The linear fitting curve of the measured temperatures and reference temperature show an R² value of 0.9999, which proves a high level of consistency and accuracy prevailing between the measured temperature and the actual temperature.

Short term Fourier transform Principal component analysis

Fast-NLM (This work)

The long-term stability of the sensors using Fast-NLM algorithm versus WD algorithm is tested. Two segments of optical fiber located at 300 m and 9.68 km positions were placed in a constant temperature oil bath. The constant temperature setpoints are set at 50 °C, 100 °C, 200 °C, and 300 °C, respectively. Each temperature setpoint was maintained for 4 hours. The measured temperatures are illustrated in Fig. 7. As shown in Fig. 7(a) and (b), the red curves, representing the measured temperature using the Fast-NLM algorithm at both near-end (300 m) and far-end (9.68 km), exhibit significantly reduced fluctuations compared to the blue curves corresponding to the WD method. At the near-end position (300 m), the Mean Square Error (MSE) values for the blue curves are 0.48 °C, 0.51 °C, 0.76 °C, and 1.02 °C, respectively while those for the red curves are 0.18 °C, 0.24 °C, 0.22 °C, and 0.42 °C, respectively. At the far-end position (9.68 km), the corresponding MSE values for blue curves are 0.76 °C, 0.78 °C, 0.76 °C, and 1.08 °C, respectively, with the red curve exhibiting values of 0.21 °C, 0.28 °C, 0.16 °C, and 0.46 °C, respectively. The corresponding long-term accuracy of temperature measurements is improved by a factor of over 2.5. As shown in Fig. 7(b) and (d), the temperature data processed by the Fast-NLM algorithm exhibit lower MSE and MD values at each test temperature point. These results demonstrate that under varying thermal conditions, the fast-NLM method outperforms the traditional approach in maintaining precision. Furthermore, the near-end (300 m) and far-end (9.68 km) results confirm that temperature measurement performance remains consistent across the entire fiber span—from short to long distances—even under low SNR conditions. And we have compared the temperature sensing measurement results obtained after algorithm processing with the Raman-DTS results reported in the existing literature, as shown in Table I. Compared to other algorithms, the integral image technology proposed in this paper enhances the real-time denoising Fast-NLM algorithm combined with the FIFO protocol. At long distances along the optical fiber, it demonstrates higher temperature accuracy and resolution while maintaining a fast response time. Additionally, the system's long-term stability is verified under both high and low temperature conditions.



20.0-100.0

30.0 - 300

Fig. 7. The sensing performance before and after Fast-NLM denoising. (a), and (c) The measured temperatures at 300 °C, 200 °C, 100 °C, and 50 °C, respectively. With time span of 4 hours, at 300 m and 9.68 km of sensing fiber. (b), and (d) The MSE and MD variation versus the temperature ranging from 50 °C to 300 °C. WD: wavelet denoising; MD: Maximum Deviation; MSE: mean squared error.

IV. CONCLUSION

We have successfully demonstrated a novel Fast-NLM real-time denoising algorithm for Raman DTS without hardware modification to conventional R-OTDR systems. The proposed method achieves a 16-fold improvement in response rate over traditional NLM methodologies while maintaining an average temperature resolution below 0.01 °C over 9.68 km. Compared with the WD algorithm, the temperature accuracy is improved from 1.59 °C to 0.39 °C at room temperature. Moreover, the temperature sensor demonstrates excellent linearity (with an R² value of 0.9999) against reference temperature and exhibits superior real-time performance during continuous temperature variations. Furthermore, the long-term accuracy of temperature

measurements is improved by a factor of over 2.5-fold versus MD method. In summary, the algorithm achieves both high temperature resolution and high-speed response under the condition of long distances and high temperatures, thus could be applied to various types of DOFS, including Raman, Rayleigh, and Brillouin scattering-based configurations, for dynamic monitoring in the realms of energy development, oil and gas exploration, and allied fields.

REFERENCES

- [1] J. Li and M. Zhang, "Physics and applications of Raman distributed optical fiber sensing," *Light Sci. Appl.*, vol. 11, 2022, Art. no. 128.
- [2] H. He et al., "Integrated sensing and communication in an optical fibre," *Light Sci. Appl.*, vol. 12, 2023, Art. no. 25.
- [3] A. Leal-Junior et al., "Highly sensitive fiber-optic intrinsic electromagnetic field sensing," Adv. Photon. Res., vol. 2, 2021, Art. no. 2000078.
- [4] F. Yang, F. Gyger, and L. Thévenaz, "Intense Brillouin amplification in gas using hollow-core waveguides," *Nature Photon*, vol. 14, no. 11, pp. 700–708, 2020.
- [5] E. F. Williams et al., "Distributed sensing of microseisms and teleseisms with submarine dark fibers," *Nature Commun*, vol. 10, 2019, Art. no. 5778.
- [6] Z. Zhan et al., "Optical polarization-based seismic and water wave sensing on transoceanic cables," *Science*, vol. 371, pp. 931–936, 2021.
- [7] F. Muñoz and M. A. Soto, "Enhancing fibre-optic distributed acoustic sensing capabilities with blind near-field array signal processing," *Nature Commun.*, vol. 13, 2022, Art. no. 4019.
- [8] M. A. Soto et al., "Evaluating measurement uncertainty in Brillouin distributed optical fibre sensors using image denoising," *Nature Commun.*, vol. 12, 2021, Art. no. 4901.
- [9] R. Jie et al., "Raman distributed optical Fiber temperature Sensing: Review of technology and applications," *Acta Opt. Sin.*, vol. 44, 2024, Art. no. 0106011.
- [10] A. Datta, H. Mamidala, D. Venkitesh, and B. Srinivasan, "Reference-free real-time power line monitoring using distributed anti-stokes Raman thermometry for smart power grids," *IEEE Sensors J.*, vol. 20, no. 13, pp. 7044–7052, Jul. 2020.
- [11] Y. Liu et al., "Global temperature sensing for an operating power transformer based on Raman scattering," Sensors, vol. 20, 2020, Art. no. 4903.
- [12] E. Ip et al., "Using Global existing Fiber networks for environmental sensing," *Proc. IEEE*, vol. 110, no. 11, pp. 1853–1888, Nov. 2022.
- [13] M. Roman et al, "Temperature monitoring in the refractory lining of a continuous casting tundish using distributed optical Fiber sensors," *IEEE Trans. Instrum. Meas.*, vol. 72, 2023, Art. no. 7000511.
- [14] M. A. Soto et al., "Distributed temperature sensor system based on Raman scattering using correlation-codes," *Electron. Lett.*, vol. 43, pp. 862–864, 2007
- [15] M. K. Saxena et al., "Raman optical fiber distributed temperature sensor using wavelet transform based simplified signal processing of Raman backscattered signals," Opt. Laser Technol., vol. 65, pp. 14–24, 2015.
- [16] M. K. Saxena et al., "Optical fiber distributed temperature sensor using short term fourier transform based simplified signal processing of Raman signals," *Measurement*, vol. 47, pp. 345–355, 2014.
- [17] A. Malakzadeh, M. Didar, and M. Mansoursamaei, "SNR enhancement of a Raman distributed temperature sensor using partial window-based non local means method," Opt. Quantum Electron., vol. 53, 2021, Art. no. 147.
- [18] M. A. Soto, A. Signorini, T. Nannipieri, S. Faralli, G. Bolognini, and F. Di Pasquale, "Impact of loss variations on double-ended distributed temperature sensors based on Raman anti-stokes signal only," *J. Light. Technol.*, vol. 30, no. 8, pp. 1215–1222, Apr. 2012.
- [19] G. D. Brinatti Vazquez, O. E. Martinez, and D. Kunik, "Distributed temperature sensing using cyclic pseudorandom sequences," *IEEE Sensors* J., vol. 17, no. 6, pp. 1686–1691, Mar. 2017.
- [20] J. Li et al., "High-accuracy distributed temperature measurement using difference sensitive-temperature compensation for Raman-based optical fiber sensing," Opt. Exp., vol. 27, 2019, Art. no. 36183.
- [21] H. Wang et al., "Research on noise reduction method of RDTS using D-SVD," Opt. Fiber Technol., vol. 48, pp. 151–158, 2019.
- [22] J. Li et al., "Slope-assisted Raman distributed optical fiber sensing," *Photon. Res*, vol. 10, no. 1, pp. 205–213, 2022.

- [23] B. Fan et al., "Realizing submeter spatial resolution for Raman distributed fiber-optic sensing using a chaotic asymmetric paired-pulse correlationenhanced scheme," *Photon. Res*, vol. 12, no. 10, pp. 2365–2375, 2024.
- [24] H. Wu et al., "Brillouin optical time domain analyzer sensors assisted by advanced image denoising techniques," *Opt. Exp.*, vol. 26, 2018, Art. no. 5126.
- [25] H. He et al., "SNR enhancement in phase-sensitive OTDR with adaptive 2-D bilateral filtering algorithm," *IEEE Photon. J.*, vol. 9, no. 3, Jun. 2017, Art. no. 6802610
- [26] M. A. Soto, J. A. Ramírez, and L. Thévenaz, "Intensifying the response of distributed optical fibre sensors using 2D and 3D image restoration," *Nature Commun.*, vol. 7, 2016, Art. no. 10870.
- [27] Y. Lv, Q. Zhu, and R. Yuan, "Fault diagnosis of rolling bearing based on fast nonlocal means and envelop spectrum," *Sensors*, vol. 15, pp. 1182–1198, 2015.
- [28] J. Su et al., "Noise suppression for phase-sensitive optical time-domain reflectometer based on non-local means filtering," *Opt. Fiber Technol.*, vol. 74, 2022, Art. no. 103119.
- [29] M. Wu, Y. Chen, P. Zhu, and W. Chen, "NLM parameter optimization for φ-OTDR signal," *J. Light. Technol.*, vol. 40, no. 17, pp. 6045–6051, Sep. 2022.
- [30] A. Buades, B. Coll, and J. M. Morel, "A review of image denoising methods, with a new one," *Multiscale Model. Simul.*, vol. 4, pp. 490–530, 2005
- [31] A. Buades, B. Coll, and J.-M. Morel, "Nonlocal image and movie denoising," Int. J. Comput. Vis., vol. 76, pp. 123–139, 2008.
- [32] P. Coupe, P. Yger, S. Prima, P. Hellier, C. Kervrann, and C. Barillot, "An optimized blockwise nonlocal means denoising filter for 3-D magnetic resonance images," *IEEE Trans. Med. Imag.*, vol. 27, no. 4, pp. 425–441, Apr. 2008.
- [33] J. Froment, "Parameter-free fast pixelwise non-local means denoising," *Image Process. Line*, vol. 4, pp. 300–326, 2014.
- [34] M. Yu et al., "Ambient condition desensitization of a fiber Raman temperature sensing system based on a dynamic sampling-correction scheme," *Appl. Opt.*, vol. 54, no. 15, 2015, Art. no. 4823.
- [35] Z. Zhang, H. Wu, C. Zhao, and M. Tang, "High-performance Raman distributed temperature sensing powered by deep learning," *J. Light. Technol.*, vol. 39, no. 2, pp. 654–659, Jan. 2021.
- vol. 39, no. 2, pp. 654–659, Jan. 2021.

 [36] H. Wang et al., "Experimental research on a Raman-based distributed temperature sensor assisted by PCA for locating the temperature abnormal event of nuclear waste drums," *Appl. Opt.*, vol. 59, 2020, Art. no. 579.

Ziheng Yan was born in Jilin, China, in 1999. He received the B.S. degree from the College of Electronic Information and Automation, Civil Aviation University of China, Tianjin, China, in 2021. He is currently working toward the Ph.D. degree with Shenzhen University, Shenzhen, China. His research focuses on distributed temperature sensors based on Raman-OTDR.

Bin Du was born in Henan, China, in 1992. He received the B.S. degree in flight vehicle propulsion engineering from the School of Astronautics, Beihang University, Beijing, China, in 2016, and the Ph.D. degree in optical engineering from Shenzhen University, Shenzhen, China, in 2021. From 2021 to 2023, he was a Postdoctoral Professor with the Guangdong and Hong Kong Joint Research Centre for Optical Fiber Sensors, Shenzhen University, where he has been an Associate Professor, since 2023. His current research interests include distributed optical fiber sensing technology, vibration sensors, and gas sensor.

Zhuoda Li was born in Inner Mongolia, China, in 1998. He received the B.S. degree in 2021 from the College of Physics and Optoelectronic Engineering, Shenzhen University, Shenzhen, China, where he is currently working toward the Ph.D. degree. His current research interests include sapphire fiber grating and optical fiber sensors.

Canxiong Chen was born in Guangdong, China, in 2002. He received the B.S. degree in 2024 from the College of Physics and Optoelectronic Engineering, Shenzhen University, Shenzhen, China, where he is currently working toward the M.S. degree. His research focuses on distributed temperature sensors.

Baijie Xu was born in Guangdong, China, in 1996. He received the B.S. degree from the College of Physics and Optoelectronic Engineering, Shenzhen University, Shenzhen, China, in 2019, and the Ph.D. degree in optical engineering from Shenzhen University, Shenzhen, China, in 2024. He is currently a Postdoctoral Fellow with the Guangdong and Hong Kong Joint Research Centre for Optical Fiber Sensors, Shenzhen University. His current research interests include distributed high-temperature sensing technology and weak fiber Bragg grating array.

Xizhen Xu was born in Guangdong, China, in 1990. He received the B.S. degree from the College of Science, Zhejiang University of Technology, Hangzhou, China, in 2013, and the M.S. and Ph.D. degrees in optical engineering from Shenzhen University, Shenzhen, China, in 2016 and 2019, respectively. From 2019 to 2021, he was a Postdoctoral Research Fellow with Shenzhen University, where he is currently an Associate Professor. He has authored or coauthored three patent applications and more than 50 journal and conference papers. His current research interests include femtosecond laser micromachining and fiber Bragg gratings.

George Y. Chen (Senior Member, IEEE, Senior Member, Optica) received the M.Eng. (bachelor's and master's joint degree) in the field of electronics and electrical engineering with computer science from Imperial College London, London, U.K., in 2009, and the Ph.D. degree from the Optoelectronics Research Centre, University of Southampton, Southampton, U.K., in 2013. From 2013 to 2015, he was a Postdoctoral Research Fellow with SPI Lasers Ltd., Industrial Research Lab. He joined the University of South Australia, Adelaide, SA, Australia, as a Research Fellow in 2015 and a Senior Research Fellow in 2019. He was a part of the MinEx CRC. In 2021, he joined Shenzhen University, Shenzhen, China, as a Professor. He is a Senior Member of Optica.

Yiping Wang (Senior Member, IEEE, Fellow, OSA) was born in Chongqing, China, in 1971. He received the B.Eng. degree in precision instrument engineering from the Xi'an Institute of Technology, Xi'an, China, in 1995, and the M.S. and Ph.D. degrees in optical engineering from Chongqing University, Chongqing, China, in 2000 and 2003, respectively. From 2003 to 2005, he was with Shanghai Jiao Tong University, Shanghai, China, as a Postdoctoral Fellow. From 2005 to 2007, he was with Hong Kong Polytechnic University, as a Postdoctoral Fellow. From 2007 to 2009, he was with the Institute of Photonic Technology, Jena, Germany, as a Humboldt Research Fellow. From 2009 to 2011, he was with Optoelectronics Research Centre, University of Southampton, Southampton, U.K., as a Marie Curie Fellow. Since 2012, he has been with Shenzhen University, Shenzhen, China, as a Distinguished Professor. He has authored or coauthored one book, 25 patent applications, and more than 420 journal and conference papers. His current research interests include optical fiber sensors, fiber gratings, and photonic crystal fibers. Prof. Wang is a Senior Member of Optical Society of America and the Chinese Optical Society.

Jun He (Member, IEEE, Member, OSA) was born in Hubei, China, in 1985. He received the B.Eng. degree in electronic science and technology from Wuhan University, Wuhan, China, in 2006, and the Ph.D. degree in electrical engineering from the Institute of Semiconductors, Chinese Academy of Sciences, Beijing, China, in 2011. From 2011 to 2013, he was with Huawei Technologies, Shenzhen, China, as a Research Engineer. From 2013 to 2015, he was with Shenzhen University, Shenzhen, China, as a Postdoctoral Research Fellow. From 2015 to 2016, he was with The University of New South Wales Sydney, Sydney, NSW, Australia, as a Visiting Fellow. Since 2017, he has been Shenzhen University, as an Assistant Professor/ Associate Professor/Distinguished Professor. He has authored or coauthored 22 patent applications and more than 132 journal and conference papers. His current research interests include optical fiber sensors, fiber Bragg gratings, and fiber lasers. Dr. He is a member of the Optical Society of America.